Advanced Devices & Instrumentation
A SCIENCE PARTNER JOURNAL

RESEARCH ARTICLE

Double-Illumination All-Optical Nanoalignment for Stacking X-Ray Fresnel Zone Plates

Siqi Wang[1], Cheng Jiang[1], Robert Peters[2], Mirwais Aktary[2], and Jinyang Liang[1]*

[1]Laboratory of Applied Computational Imaging, Centre Énergie Matériaux Télécommunications, Institut National de la Recherche Scientifique, Université du Québec, Varennes, QC J3X1P7, Canada. [2]Applied Nanotools Inc., Edmonton, AB T6G2M9, Canada.

*Address correspondence to: jinyang.liang@inrs.ca

Citation: Wang S, Jiang C, Peters R, Aktary M, Liang J. Double-Illumination All-Optical Nanoalignment for Stacking X-Ray Fresnel Zone Plates. *Adv. Devices Instrum.* 2025;6:Article 0088. https://doi.org/10.34133/adi.0088

Submitted 5 December 2024
Revised 6 February 2025
Accepted 10 February 2025
Published 2 May 2025

Fresnel zone plate (FZP) stacking is an approach to enhance diffraction efficiency in x-ray focusing and imaging by physically aligning 2 or more FZPs to increase the effective thickness and optical efficiency. Existing methods face limitations in x-ray-source availability, controlled degrees of freedom, alignment accuracy, and contact-induced friction. To overcome these limitations, we develop a double-illumination all-optical nanoalignment (DIANA) system. Designed to leverage the x-ray FZP chip's nanopatterned characteristics, DIANA uses coherent illumination in reflection mode to implement laser interferometry for accurate tilt and yaw adjustment. It also employs incoherent illumination in transmission mode for high-contrast nanoalignment using Vernier/main scales and moiré fringes. Using DIANA, we demonstrate the stacking of 2 x-ray FZPs with under 30-nm alignment accuracy.

Introduction

Fresnel zone plates (FZPs) are diffractive optical elements used for x-ray focusing and imaging [1]. Fabricated on an x-ray transparent membrane (e.g., Si_3N_4 and SiC), they are composed of concentric circular Fresnel zones alternating between being transparent and opaque [2]. The incident x-ray beam, diffracted by the opaque zones made from high-Z-number and phase-shifting materials (e.g., Au, Ni, Pt, and W), can be focused on certain distances by constructive interference. Compared to other x-ray focusing optics (e.g., compound refractive lenses [3,4], capillary optics [5,6], Kirkpatrick–Baez mirrors [7,8], and multilayer Laue lenses [9,10]), FZPs offer a much more compact solution with a comparable spatial resolution [11]. Thus, they have become key x-ray optical components for diverse applications [12], including advanced instrumentation [13–15], nanolithography [16], and astronomy [17].

Among the technical parameters of an FZP, diffraction efficiency is of great importance. Highly efficient FZPs can largely decrease the acquisition time, which enables faster experiments and thus reduces radiation damage to specimens [18,19]. To accomplish this goal while maintaining a high spatial resolution, especially in the hard x-ray region, an FZP is required to have high-aspect-ratio structures, with the outermost zone widths comparable to the desired resolution of the system [20]. However, high-aspect-ratio zones required for high efficiency and high resolution often exceed the fabrication capability of nanolithography [21], resulting in the bending, distortion, and/or collapse of spatial structures. This constraint limits the diffraction efficiency of FZPs in the soft x-ray regime, rapidly further decreasing toward the hard x-ray range [22].

Various nanofabrication techniques have been developed to produce high-aspect-ratio FZPs [23]. For example, multilayer FZPs can be fabricated by sequentially coating a cylindrical substrate (e.g., a glass fiber [24] and a capillary lumen [25]) via atomic layer deposition of high-Z-number and low-Z-number materials with proper thicknesses according to the Fresnel zone widths, followed by focus-ion-beam slicing [26–28]. Although capable of producing hundreds-to-one aspect ratios on tens-of-nanometer spatial features [29], this method requires demanding thickness control in the deposition processes. Limited by the slow deposition speed, the produced FZPs often have a relatively small aperture size, resulting in a short working distance that impedes their applicability [30]. To obtain a large aperture and a high aspect ratio, conventional electron beam lithography has been teamed up with metal-assisted chemical etching to deep-etch silicon with a >100:1 aspect ratio [31]. Nonetheless, using silicon as a scaffold can lead to high x-ray absorption.

An attractive alternative to increase the structure thickness is FZP on-chip stacking [32]. If aligned laterally to within one-third of the width of the outermost zone and longitudinally within the optical near field, these stacked FZPs can be considered a single optical element of larger effective thickness [31]. This approach can be directly realized by repeating the existing nanostructuring processes of electron beam lithography, reactive ion etching, and electroplating [33,34]. In principle, the achievable aspect ratio is limited only by the number of FZPs that can be accurately stacked. In practice, however, the requirement of many steps makes this approach vulnerable to fabrication issues. To overcome this limitation, FZPs can be fabricated on each side of the membrane [35]. Despite simplifying the fabrication complexity, double-sided FZPs are subject to a potential scaling issue,

possibly induced by the shrinkage of the used low-Z-number material during fabrication [36].

Besides using sophisticated fabrication-based stacking techniques, a more direct approach is to align and stack multiple standard FZPs [37]. Without disrupting the mature fabrication procedure, this approach leverages the high availability and high quality of standard FZPs. The alignment can be performed by using x-ray phase-contrast microscopy [38]. In particular, the x-ray transmitted through the FZP stack is filtered by an order-sorting aperture. The selected first-order diffraction is converted by a scintillator to visible light, which is then recorded by an optical microscopy setup. FZPs can be accurately stacked by monitoring the location of the first diffraction order [39] or imaging the x-ray interference [31,40]. Since its first success in the early 2000s [18], x-ray-based FZP stacking has made substantial development [39–42]. A stack of up to 6 FZPs has been demonstrated, which improves the diffraction efficiency by 15.7 times at 27 keV compared to the single-FZP counterpart [41]. However, x-ray light sources, especially synchrotrons, have high operation expenses and limited availability. They also require sophisticated training and equipment handling in a working environment in which ionized radiation could pose potential harm to health. All these limitations have increasingly hindered the further development and mass implementation of x-ray-based FZP stacking.

The limitations imposed by x-rays can be circumvented by optical nanoalignment using visible light [43–45]. A key tool that supports detecting nanometer-level movement is moiré fringes [46]. Manifesting the beat frequency in space, moiré fringes allow sensing diminutive displacement beyond the optical diffraction limit [47]. This method is also universally applicable to diverse types of light sources. These salient features for highly sensitive displacement detection have propelled the widespread implementation of moiré fringes as an accurate alignment approach in advanced lithography [48–50]. Integrated into many instruments of nanoimprint lithography [51] and proximity lithography [52], moiré-fringe-based metrology has reached an alignment accuracy of tens of nanometers [53]. Nonetheless, existing optical moiré-fringe-based alignment systems confront difficulties for x-ray FZP stacking. First, most of the techniques, implemented on lithography apparatus, are in reflection mode. Due to the high optical reflection of high-Z-number materials, the produced moiré fringes have low contrast and hence a reduced alignment accuracy. Meanwhile, despite offering highly sensitive measurement in the lateral displacement, moiré fringes face challenges in sensitivity for tilt–yaw adjustments, requesting auxiliaries. An attempt distributed 10-μm-diameter microbeads on the edge between 2 FZP chips and pressed the 2 chips to touch for parallelism [54]. However, due to the lack of optical feedback, the alignment accuracy of the tilt–yaw adjustment was not verified. More importantly, the contact of microbeads to both chips induced friction during lateral adjustment, which led to limited alignment accuracy and potential chip damage.

To surmount these problems, we develop double-illumination all-optical nanoalignment (DIANA) for contactless stacking of 2 hard x-ray FZP chips. Leveraging the highly reflected seed layer on the FZP chip, laser interferometry is employed in reflection mode for tilt–yaw adjustment with a 0.3-mrad accuracy. Quadruple moiré-fringe alignment, assisted by geometric image alignment, is implemented in transmission mode to achieve an alignment accuracy of under 30 nm in the x and y directions and 100 μrad in rotation.

Materials and Methods

Configuration of the FZP chips

The sizes of the top FZP chip and the bottom FZP chip are 4 mm × 4 mm and 5 mm × 5 mm, respectively. A side-view schematic of these chips is shown in Fig. 1A. A 400-μm-thick Si substrate is used as the handle. A 2 mm × 2 mm square window is hollowed out in the middle to maintain a sufficiently large area for patterning. A 1-μm-thick Si_3N_4 film is deposited above the Si handle. Above the Si_3N_4 layer, a 3-nm-thick Cr layer and a 15-nm-thick Au seed layer are plated to connect and support all spatial features made of Au with a height of 0.7 to 0.8 μm.

Top-view schematics of the top chip and the bottom chip are shown in Fig. 1B and C, respectively. On each chip, an FZP with a 310-μm diameter and a 100-nm-wide outermost zone is placed in the center. Alignment patterns and markers, whose design rationale is detailed in the next section, are added to the periphery. In particular, gratings with periods of $P_{1i} = 2.42$ μm, $P_{2i} = 2.58$ μm, $P_{1o} = 2.46$ μm, and $P_{2o} = 2.54$ μm are placed in the inner and outer areas of both chips to generate moiré fringes (see details in Table 1). At 4 sides of the periphery of the top chip are Vernier scales [55] with the smallest division of 15 μm. The midpoints of these Vernier scales are aligned with the FZP center. Correspondingly, on the bottom chip, the main scales are placed with the smallest division of 15.5 μm. At the 4 corners, anti-cross markers with a gap of 12 μm are placed on the top chip, and cross markers with a width of 10 μm are placed on the bottom chip.

Design rationale of the FZP chips

The overall goal of alignment is to stack the 2 FZP chips face to face in proximity with an accuracy of one-third of the finest spatial feature [56], which requires an accuracy of ~30 nm for the FZPs used in this work. To achieve this goal, we intend to adjust 5 degrees of freedom—namely, x, y, rotation, tilt, and yaw. In particular, the tilt and yaw are adjusted to reduce the misalignment to less than 5 mrad. In the z direction, this level of parallelism produces a scaling error of a few nanometers over the patterned area, which is negligibly small to affect the x and y alignment accuracy. This step also enables reducing the interchip distance to the tens-of-micrometer level. At this proximity, both chips can be clearly imaged, which is essential for the execution of the ensuing steps. Then, the x, y, and rotation are adjusted in a coarse alignment by using both the 4 cross/anti-cross markers and the Vernier/main scales so that the misalignments are reduced to ±0.5 μm, ±0.5 μm, and ±1.25 mrad, all of which are within the measurement range of moiré fringes. These 3 degrees of freedom are further controlled in a fine alignment by using moiré patterns to achieve an accuracy of 30 nm in the x and y directions and 100 μrad in rotation.

To produce suitable moiré fringes, 2 one-dimensional gratings with similar pitches are designed for the FZP chips. In particular, their superposition modulates the transmitted light with a spatial pitch related to the difference in the frequencies of both gratings [57]. The minimum interchip distance is set to be 10 μm to protect the fine spatial features on both chips. Considering the Talbot effect, the gratings' averaged pitch is calculated to be 2.5 μm.

To obtain the relative displacement of the 2 FZP chips along the direction perpendicular to the grating grooves, a pair of gratings on both chips is necessary. On one chip, 2 gratings are placed adjacently along the direction of the grating grooves.

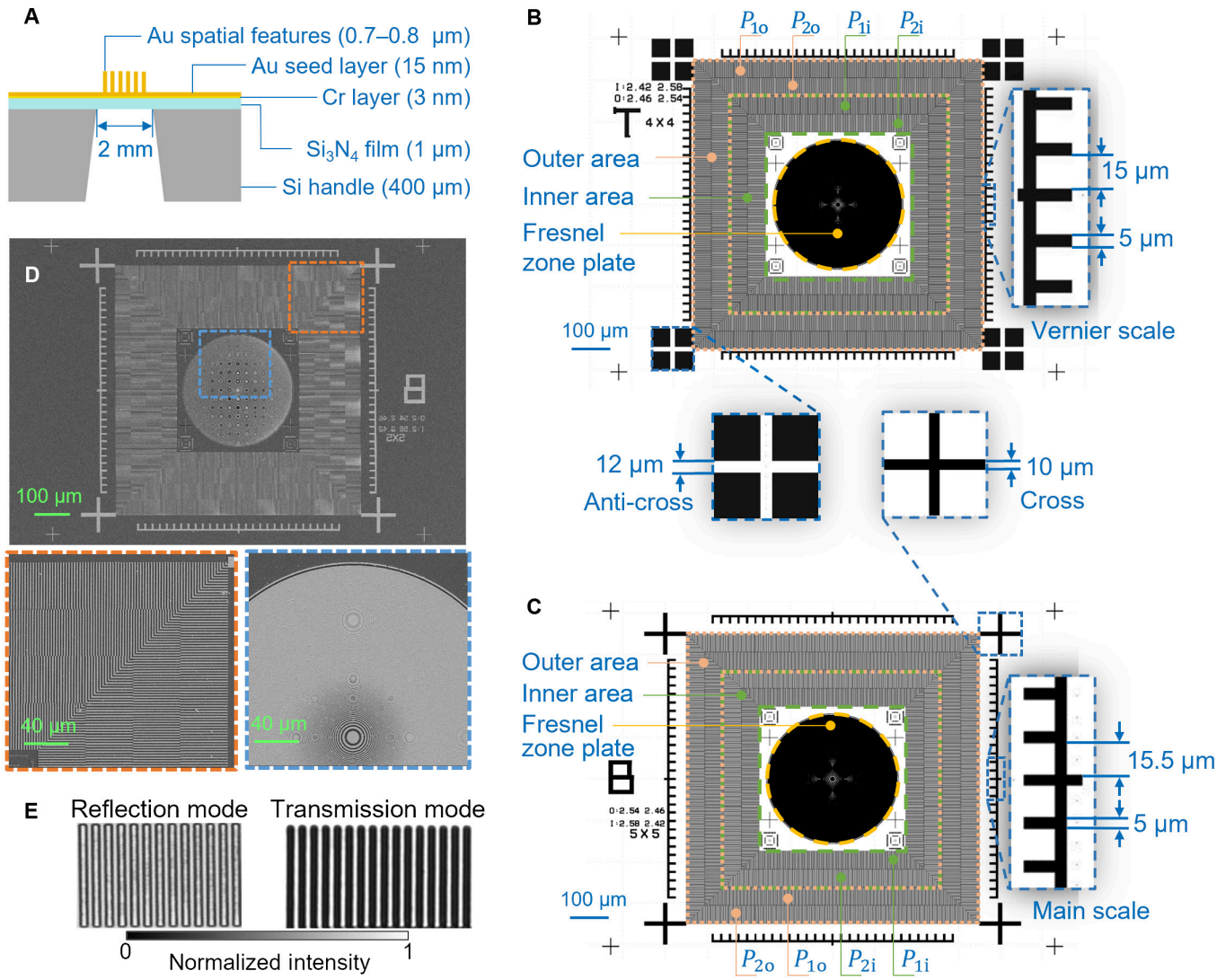

Fig. 1. Design and fabrication of the Fresnel zone plate (FZP) chips. (A) Side-view schematic. (B and C) Top-view schematics of the designed patterns on the top (B) and the bottom (C) FZP chips. P_{1i}, P_{2i}, P_{1o}, P_{2o}, periods of gratings in the inner and outer areas. (D) Scanning electron microscopy images of a fabricated bottom FZP chip with a magnification ratio of ×86 (top) and 2 local areas marked by the blue and orange boxes in the top image with magnification ratios of ×377 (bottom left) and ×383 (bottom right). (E) Optical microscopy images of a local area of a fabricated grating on the FZP chip in reflection mode (left) and transmission mode (right).

Table 1. Specifications of the grating pairs designed for the FZP chips (j = i or o)

Parameters	Inner area	Outer area
Pitch (spatial frequency) of grating 1	$P_{1i} = 2.42$ μm (413.2 lp/mm)	$P_{1o} = 2.46$ μm (406.5 lp/mm)
Pitch (spatial frequency) of grating 2	$P_{2i} = 2.58$ μm (387.6 lp/mm)	$P_{2o} = 2.54$ μm (393.7 lp/mm)
Pitch (spatial frequency) of moiré fringes [a]	$P_{mi} = 39$ μm (25.6 lp/mm)	$P_{mo} = 78$ μm (12.8 lp/mm)
Magnification ratio of moiré fringes [b]	$M_{mi} = 31.25$	$M_{mo} = 62.5$
Measurement range of moiré fringes [c]	$R_{mi} \in [-0.624, 0.624]$ μm	$R_{mo} \in [-0.624, 0.624]$ μm

[a] $P_{mj} = P_{1j}P_{2j}/|P_{1j} - P_{2j}|$.
[b] $M_{mj} = (P_{1j} + P_{2j})/|P_{1j} - P_{2j}|$.
[c] $R_{mj} \in 0.5 \times [-P_{mj}/M_{mj}, P_{mj}/M_{mj}]$.

On the other chip, the 2 gratings switch their positions. Their superposition generates 2 sets of moiré fringes with the same pitch. In case of a lateral displacement between the 2 chips, the 2 sets of moiré fringes shift in opposite directions. As shown in Table 1, by measuring the displacement Δ_j and using the magnification ratio of the moiré fringes M_{mj}, the misalignment is calculated by $\delta_j = \Delta_j / M_{mj}$, where $j = \mathrm{i}$ or o specifies the inner or the outer area, respectively.

The grating pitches of the inner area (i.e., P_{1i} and P_{2i}) and the outer area (i.e., P_{1o} and P_{2o}) are determined by comprehensively considering the magnification ratio (i.e., M_{mj}) and the pitch of the moiré fringes (denoted by P_{mj}). The corresponding spatial frequencies are the inverse of the pitches of the gratings and moiré fringes. A smaller difference between the 2 grating pitches increases both parameters simultaneously, which enhances the misalignment detection ability in data acquisition while reducing the information extraction ability in the postprocessing. Thus, 2 pairs of gratings with different pitch combinations are placed in the inner and outer areas to evaluate alignment accuracy (see Table 1 for details).

Fabrication of FZP chips

The designed FZP chips were fabricated by using 100-keV electron beam lithography. The high-quality nanoscale features were verified by using scanning electron microscopy (Fig. 1D). Moreover, the gratings were examined under an optical microscope in both reflection mode and transmission mode. The former revealed a high reflection of both the gratings and the Au seed layer. As a result, the intensity difference could be observed only at the groove boundaries (left panel of Fig. 1E).

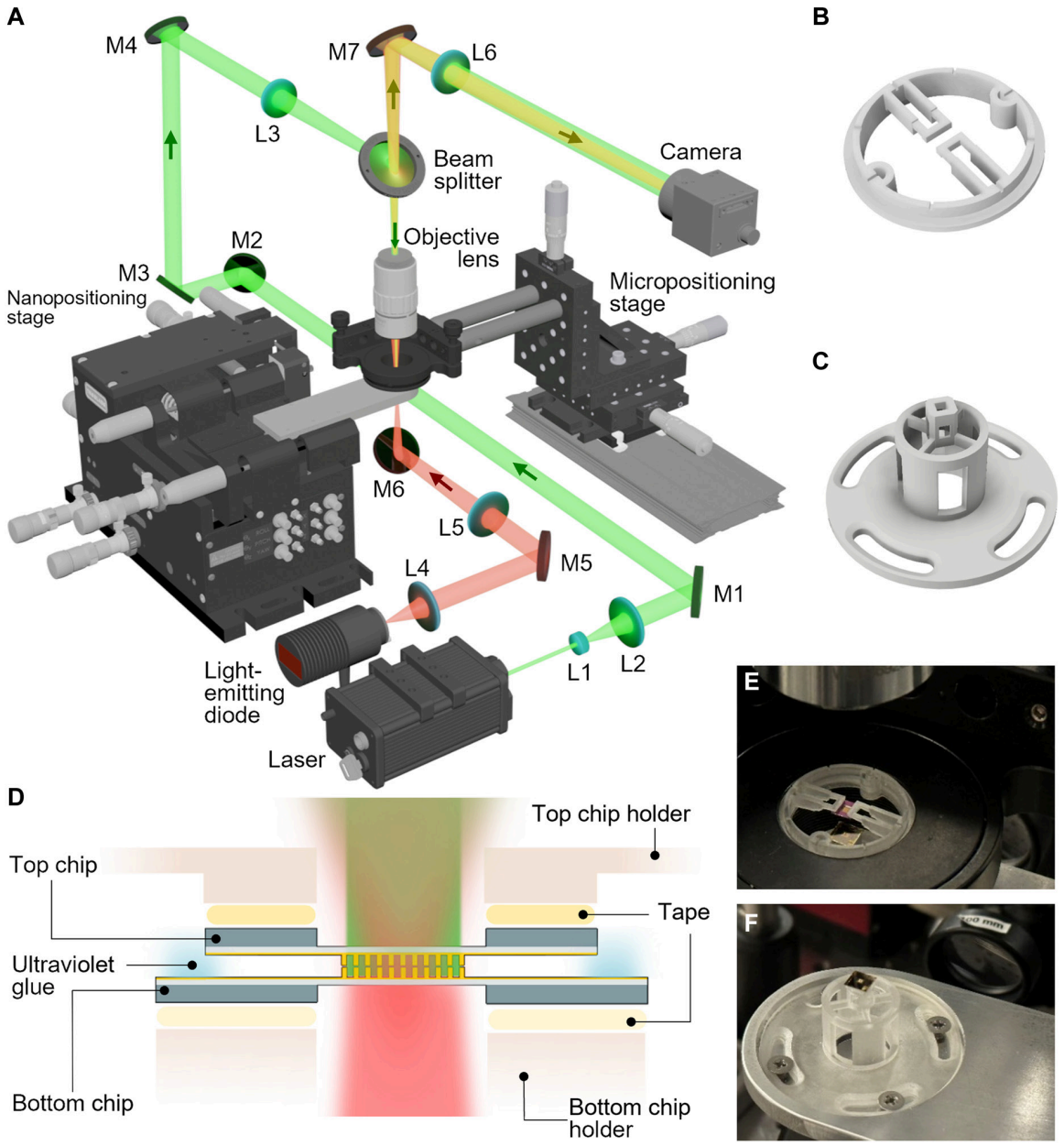

Fig. 2. Double-illumination all-optical nanoalignment (DIANA). (A) System schematic. L1 to L6, lenses; M1 to M7, mirrors. (B and C) Design of the holders for the top (B) and the bottom (C) FZP chips. (D) Side-view configuration of chip holding. (E and F) Photos of the loaded top (E) and bottom (F) FZP chips.

In contrast, complete grating grooves could be seen in transmission mode, as shown in the right panel of Fig. 1E. These results suggested that for the x-ray FZP chips, high-contrast moiré fringes could be produced by using the transmission mode, while high-contrast interference patterns could be produced by using the reflection mode.

Results

System

Double-illumination all-optical nanoalignment

Based on the requirements of nanoalignment and the characterization of the fabricated FZP chips, we designed and constructed the DIANA system, which is schematically shown in Fig. 2A. The DIANA system consists of 4 parts—an optical microscope with incoherent and coherent light sources, motion control modules, precise supports for both FZP chips, and auxiliary components for chip gluing.

The coherent light source is a continuous-wave laser at $\lambda_c = 532$ nm (CNI, MGL-III-532-200mw). After expansion and collimation using lenses L1 (Thorlabs, LC2265) and L2 (Thorlabs, LA1433), the beam is directed by mirrors M1 to M4, passes through tube lens L3 (Thorlabs, LA1708), and is reflected by a beam splitter (Thorlabs, CM1-BP145B1) to generate a focus on the back focal plane of a long working distance ×10 objective lens (Thorlabs, MY10X-803) mounted with a kinematic mount (Thorlabs, KC1XY) with ±4° tilt and yaw adjustment. This scheme produces wide-field illumination with a 2-mm-diameter field of view (FOV) to the FZP chips for reflection-mode imaging. Meanwhile, the DIANA system incorporates incoherent illumination of a light-emitting diode with a central wavelength of $\lambda_{ic} = 617$ nm (Thorlabs, M617L5) working in transmission mode. The diverging output beam passes through lenses L4 (Thorlabs, LA1509) and L5 (Thorlabs, LA1433) to illuminate the chips with an FOV the same as that of coherent illumination in size. The reflected coherent illumination or the transmitted incoherent illumination is collected by the same objective lens, transmitted through the beam splitter and tube lens L6 (Thorlabs, AC254-200-A-ML) to form an image of the object on a complementary metal–oxide–semiconductor camera (Edmund Optics, BFS-U3-200S6M-C).

To accurately position the 2 FZP chips facing each other, the DIANA system employs a homebuilt 6-axis micropositioning stage for the top chip and a 6-axis nanopositioning stage (Thorlabs, MAX603D) for the bottom chip. The top chip is glued onto a 3-dimensionally printed holder (Fig. 2B) by 2 small pieces of double-sided tape. The holder is placed in a 4-axis rotation mount (Thorlabs, KS1RS), providing 360° rotation adjustment and a ±4° tilt–yaw adjustment. The 4-axis rotation mount is attached to an x–y–z translation stage (Keenso, SEMX80-AS) with a 25-mm linear travel range. This assembled 6-axis micropositioning stage is placed on a rail (Thorlabs, XT95SP-500) to conveniently load the top chip.

The bottom chip is glued onto another 3-dimensionally printed holder (Fig. 2C) by a piece of double-sided tape. This holder is attached to an extension plate connected to the nanopositioning

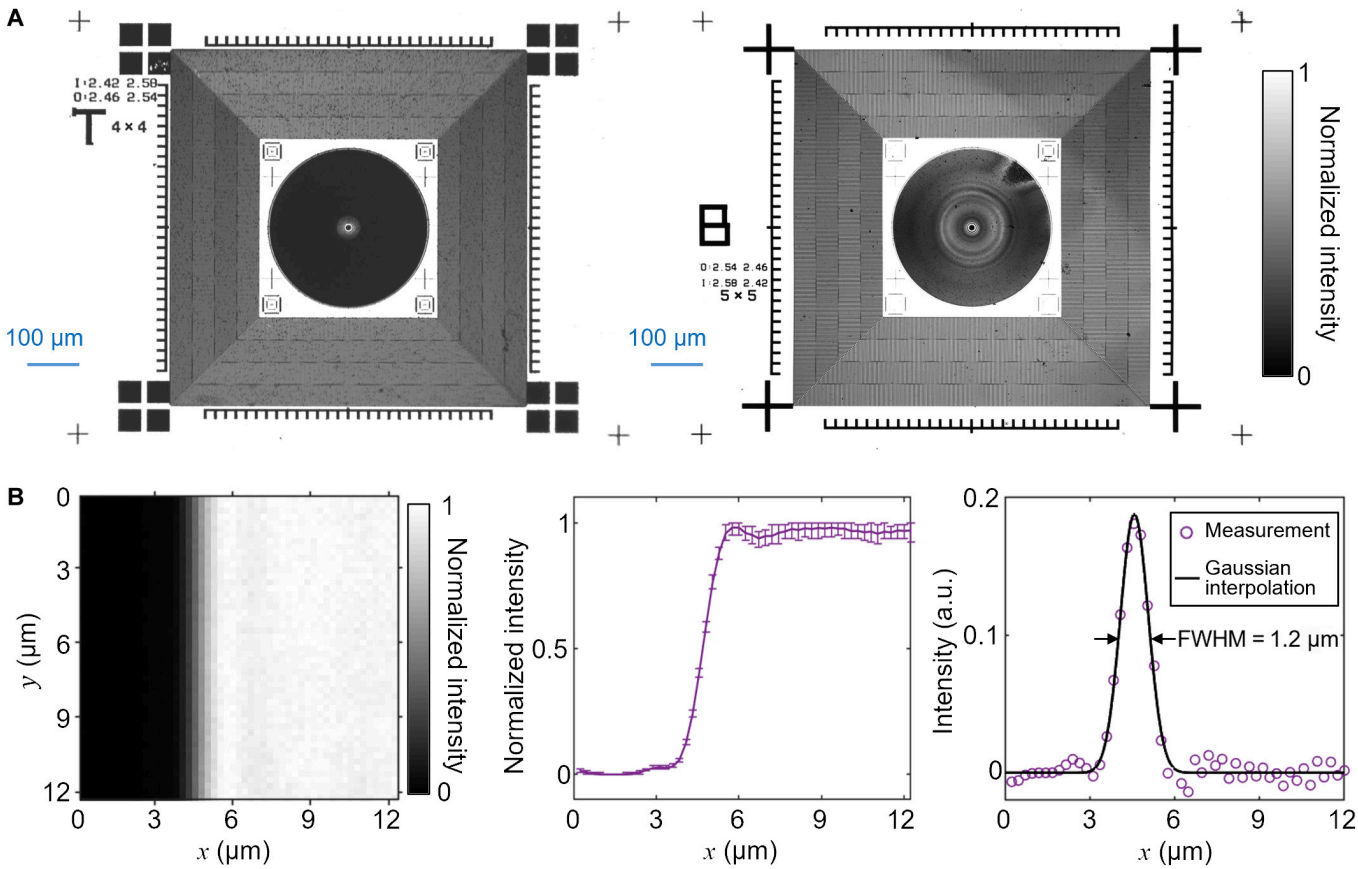

Fig. 3. Quantification of the double-illumination all-optical nanoalignment (DIANA) system's performance. (A) Images of the top (left) and bottom (right) FZP chips under incoherent illumination. (B) Evaluation of spatial resolution. Left: Image of an edge. Middle: Averaged edge spread function. Error bar: standard deviation. Right: Line spread function with Gaussian interpolation. FWHM, full width at half maximum.

stage, which provides an accuracy of 1 nm for the translation motions in the x, y, and z directions and 0.018 μrad for the tilt, yaw, and rotation adjustments. A schematic of the 2 chips connected to the holders under both illuminations is shown in Fig. 2D, and photos of loaded chips are shown in Fig. 2E and F. After the alignment, the 2 chips are glued by using an ultraviolet (UV) light adhesive to produce the stacked unit.

Evaluation of the DIANA system's performance

The evaluation started by using incoherent illumination to inspect the imaging quality of fabricated FZP chips. As shown in Fig. 3A, both chips can be clearly imaged by the DIANA system. To quantify the spatial resolution, an edge of a spatial feature on the bottom chip was imaged, shown in the left image of Fig. 3B. The averaged edge spread function ESF in the x axis was analyzed, and the standard deviation was calculated, shown in the middle image of Fig. 3B. Then, the line spread function was obtained by taking the derivative of the edge spread function. Fitted by Gaussian interpolation, the full width at half maximum of this line spread function was calculated to be 1.2 μm, which represents the system spatial resolution (right image of Fig. 3B). Using the spatial resolution as the criterion and the grating specifications (see Table 1), the theoretical alignment accuracy was estimated to be 38.3 nm for the inner area and 19.2 nm for the outer area.

Alignment procedure

Tilt–yaw alignment

As the first step in this procedure, tilt and yaw were adjusted by using laser interferometry. Under the coherent illumination in reflection mode, the highly reflective Au seed layer on both chips generated interference fringes of equal inclination. The tilt (or yaw) misalignment angle was calculated by $\gamma = N\lambda_c / 2w$, where N is the number of the fringes in the x or y direction and w is the length (or width) of the FOV.

Representative results for this step are shown in Fig. 4. First, by adjusting the micropositioning stage, the misalignments were reduced to 4.4 mrad for tilt and 3.1 mrad for yaw (Fig. 4A). Then, the alignment was performed by tuning the nanopositioning stage until no fringes of equal inclination can be seen in the FOV (Fig. 4B and C). The tilt and yaw misalignments were calculated to be 0.3 and 0.2 mrad, respectively, indicating that the depth difference over the FOV was within $\lambda_c / 2$. This level of parallelism could induce only a subnanometer projection distortion in the x and the y directions within the targeted FOV, thus satisfying the alignment accuracy.

Coarse alignment for x, y, and rotation

Misalignments in x, y, and rotation are defined to describe the relative displacement of the top chip to the bottom chip. This convention is reflected by the coordinate system shown in Fig. 5A. The coarse alignment was started by adjusting x, y, and rotation in sequence to align the crosses on the bottom chip with the anti-crosses on the top chip in 4 corners. To quantitatively evaluate the alignment accuracy, in Fig. 5B, we plot the normalized intensity of 8 selected line profiles (marked as l_i to l_{viii} in Fig. 5A). These intensity profiles are not symmetric with respect to the bar center on the corresponding crosses, indicating position mismatches between the crosses and anti-crosses. The alignments of x, y, and rotation were performed

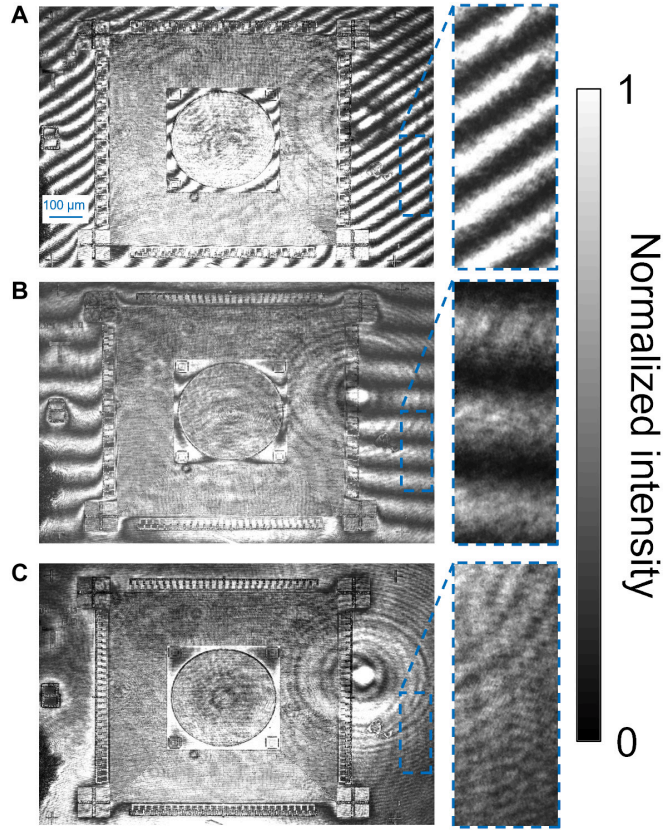

Fig. 4. Laser interferometry for tilt–yaw alignment. (A) Interference fringes produced by misalignment in both tilt and yaw. (B) Interference fringes produced by misalignment only in yaw. (C) Interference pattern after completing the tilt–yaw alignment.

iteratively until the summation of the intensity difference in all line profiles was minimized.

Second, using custom alignment calculation and control software (detailed in Note S1 and Fig. S1), Vernier scales on the top chip and main scales on the bottom chip on 4 sides were used to automatically adjust the position of the 2 chips. Eight selected line profiles, centered by the midpoints of the Vernier/main scales (marked as l_1 to l_8 in Fig. 5A), were analyzed in pairs. The edges of the spatial features in these line profiles were obtained by differentiation (Fig. 5C). The most precisely aligned Vernier/main scale pair was determined by averaging the deviation between each pair of peaks of the red and blue lines. The position deviations on all 4 sides were calculated to be −0.2 μm (top), −1.7 μm (right), 1.2 μm (bottom), and 0 μm (left) with an ±0.5 μm uncertainty determined by the difference between the smallest division of the main scale (i.e., 15.5 μm) and that of the Vernier scales (i.e., 15 μm). In this way, the misalignments in x, y, and rotation were determined to be 0.50 μm, −0.85 μm, and −2.04 mrad, respectively. After several rounds of adjustments, the misalignments in x and y were reduced to be within ±0.5 μm and the rotation misalignment within ±1.25 mrad, which satisfied the goals of coarse alignment.

Fine alignment for x, y, and rotation

After the coarse alignment, the fine alignment with the goal of 30-nm accuracy was performed by analyzing the moiré fringes generated by the grating pairs in the inner and outer areas. We first cropped out the moiré fringes from both areas on all 4

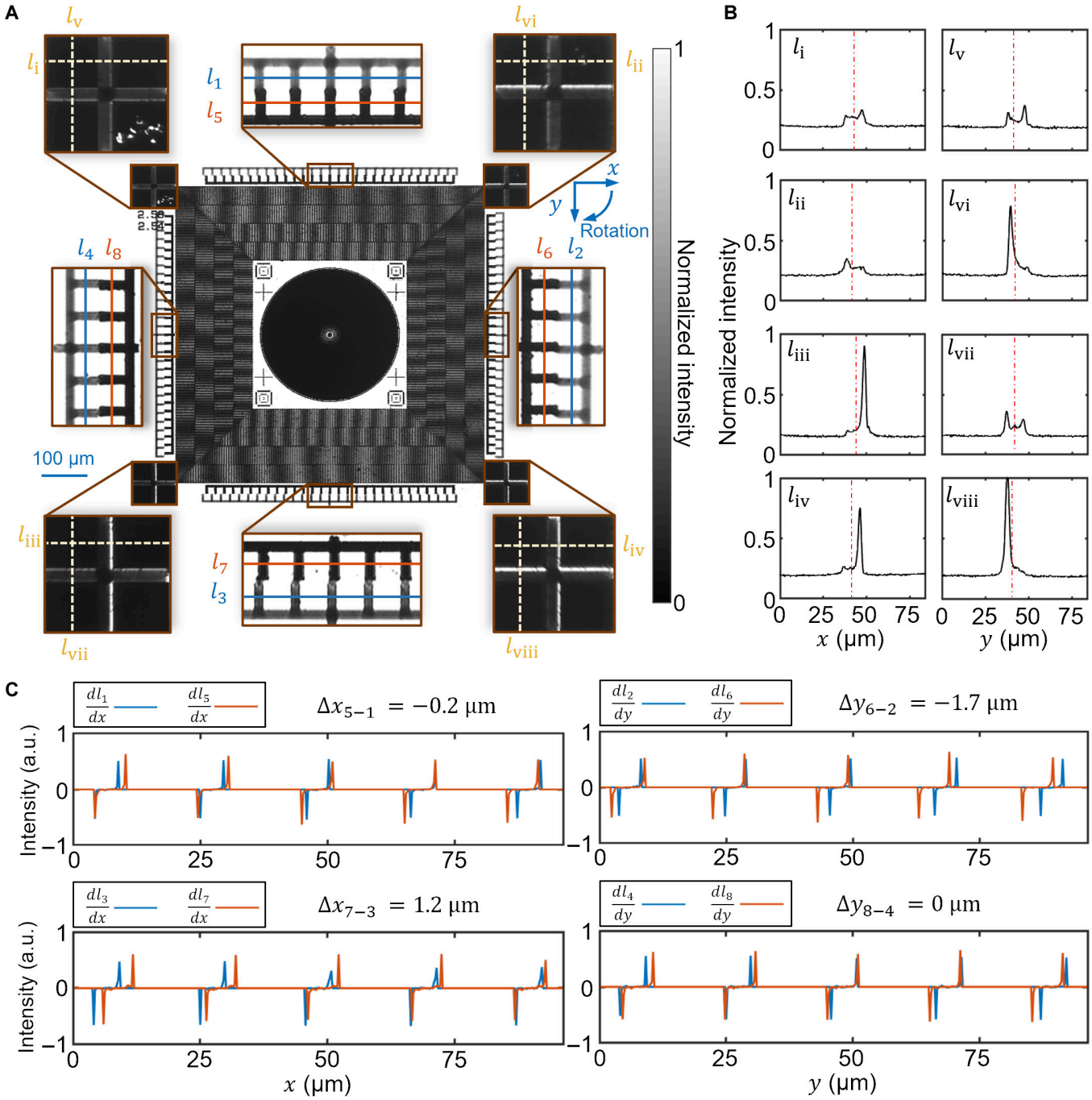

Fig. 5. Analysis of coarse alignment of x, y, and rotation. (A) Representative image of 2 stacked FZP chips during the alignment. I_i to I_{viii}, line profiles of the crosses and anti-crosses; I_1 to I_4, line profiles of the main scales; I_5 to I_8, line profiles of the Vernier scales. (B) Analysis of line profiles I_i to I_{viii}. (C) Analysis of spatial differentiation of line profiles I_1 to I_8 in pairs.

sides. Two examples are shown in the insets of Fig. 6A. Then, the intensity profiles of the moiré fringes were obtained by averaging the cropped images along the direction parallel to the grating grooves (Fig. 6B). These curves were Fourier transformed [58,59]. In the example shown in Fig. 6C, the peak at 13.2 lp/mm is produced by the moiré fringes, while the peaks at 390.4 and 403.7 lp/mm are matched with the specifications of the corresponding 2 gratings in the outer area (see Table 1). To improve the accuracy of moiré-fringe extraction, the Fourier spectra were low-pass filtered by a Butterworth filter with no phase modulation (Fig. 6C). The filtered result (shown as the dotted lines Fig. 6B) were further fitted by single-frequency sinusoids (shown as the green and black solid lines in Fig. 6B), whose period was given by the extracted moiré fringes. The experimental verification of the capability of this approach to sense nanometer-level displacement is detailed in Note S2 and Fig. S2.

In the ensuing analysis, we calculated the phase differences (denoted by $\Delta\varphi_j$) between the moiré fringes in the inner and outer areas, which were transferred to the measured misalignment by $\Delta_j = \Delta\varphi_j P_{mj}/2\pi$. In this example, the phase difference of moiré fringes was calculated to be −0.61 rad, which

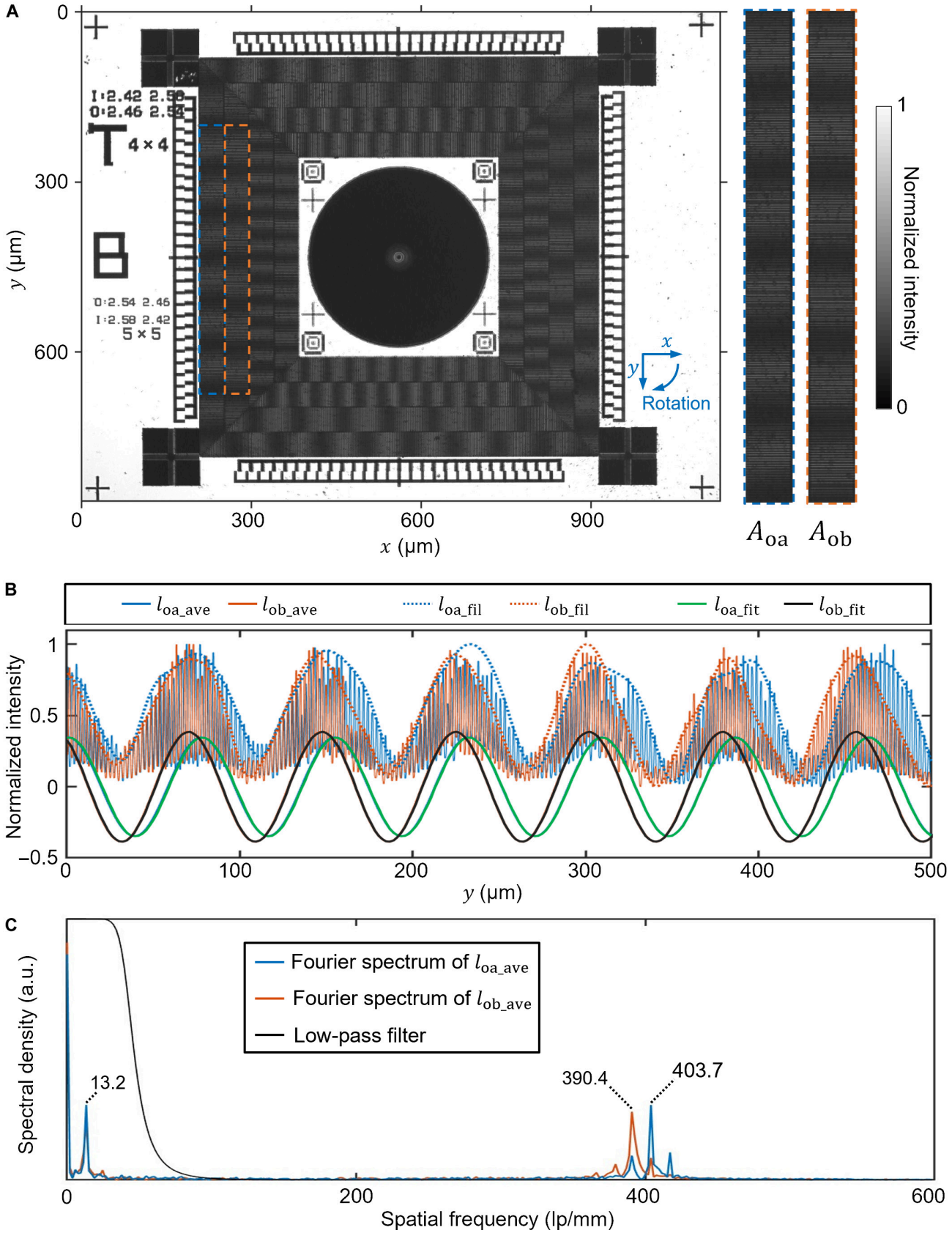

Fig. 6. Analysis of the fine alignment of x, y, and rotation. (A) Two stacked FZP chips during fine alignment. Insets: Zoom-in views of 2 cropped grating areas A_{oa} and A_{ob} in the left region showing moiré fringes. (B) Line profiles used in the fine alignment analysis for the selected areas in (A). I_{oa_ave} and I_{ob_ave}, averaged line profiles; I_{oa_fil} and I_{ob_fil}, line profiles by low-pass-filtering I_{oa_ave} and I_{ob_ave}; I_{oa_fit} and I_{ob_fit}, line profiles by using sinusoidal fitting of I_{oa_fil} and I_{ob_fil} without the dc term. (C) Fourier spectra of I_{oa_ave} and I_{ob_ave} with the employed low-pass filter.

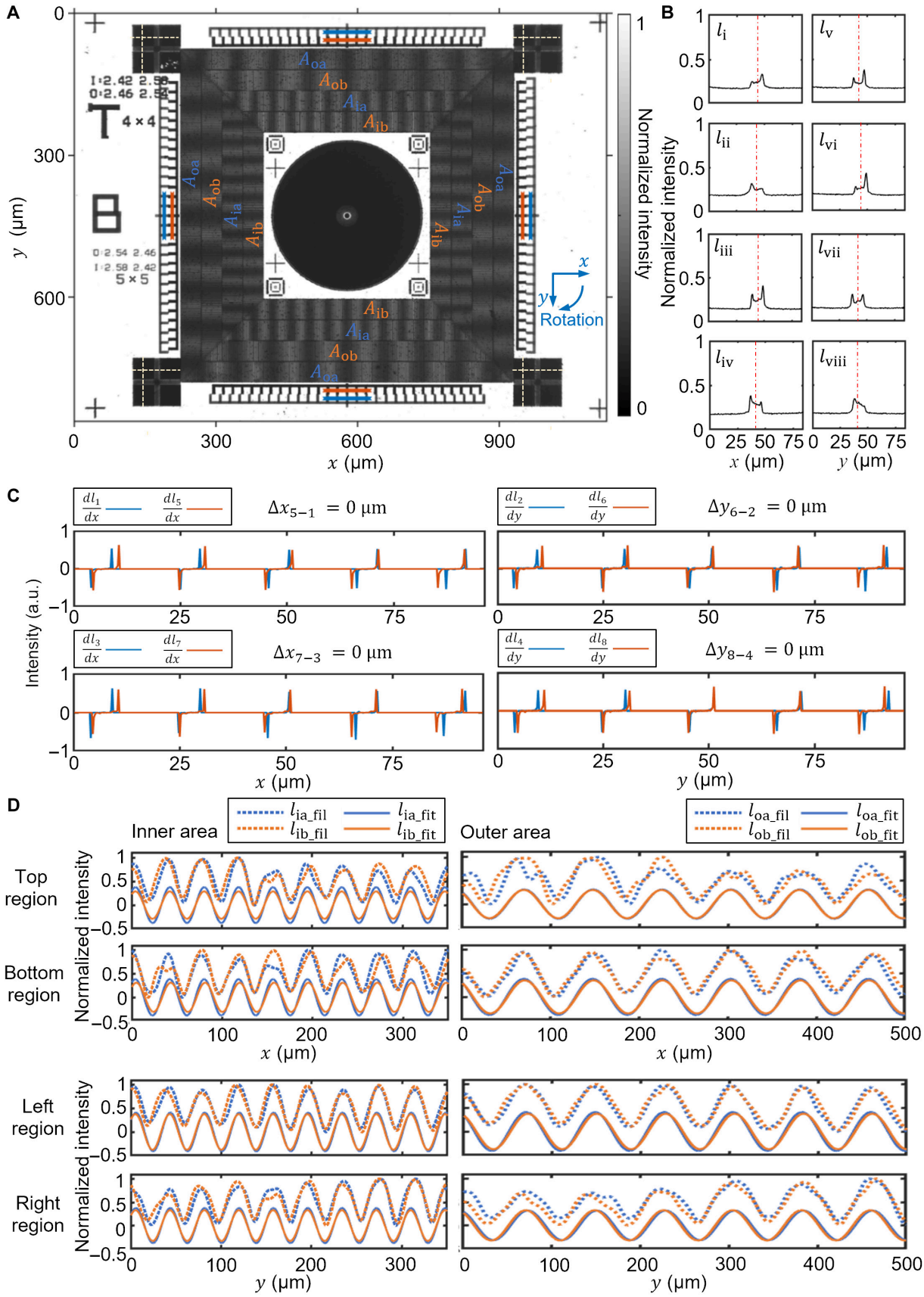

Fig. 7. Analysis of aligned FZP chips. (A) Image of 2 aligned chips. A_{ia} and A_{ib}, selected regions from the inner area for moiré-fringe analysis. (B) Cross-sections of the corner crosses. (C) Spatial differentiation of the lines of main scales and the Vernier scales marked in (A). (D) Fringe extractions of the inner and outer areas. I_{ia_fil}, I_{ib_fil}, I_{ia_fit}, and I_{ib_fit} have the same meaning as I_{oa_fil}, I_{ob_fil}, I_{oa_fit}, and I_{ob_fit} in Fig. 6 but are for selected regions from the inner area.

corresponds to a mismatch of −7.48 μm from A_{ob} compared to A_{oa}. Hence, the misalignment was determined to be −120 nm. The same process was performed with the right, top, and bottom regions of the outer area, which yielded misalignments of −387, 335, and 628 nm, respectively. By averaging the misalignment in the left and right regions, the *y* misalignment was obtained to be −254 nm. Similarly, the *x* misalignment was calculated by averaging the top and bottom regions to be 482 nm. Finally, the rotation misalignment was calculated by the difference between the left and right (or top and bottom) misalignments and divided by the distance between the 2 regions (i.e., 619 μm), which yielded −0.43 mrad (or −0.47 mrad for the top and bottom regions). The same calculations were made based on the inner regions to demonstrate the credibility of the obtained data. These misalignment results were used as feedback to the nanopositioning stage for adjusting the bottom chip's position accordingly. Using the alignment calculation and control software (see Note S1 and Fig. S1), several rounds of *x*, *y*, and rotation alignment were performed until the moire fringes in both the inner and outer areas were aligned on all 4 sides.

Analysis of aligned FZP chips

The quality of alignment was analyzed by using all criteria established for the coarse and fine alignments. An example of aligned chips is shown in Fig. 7A. The cross-section profiles of the 4 corners show balanced peaks (Fig. 7B), suggesting that all crosses were aligned with anti-crosses. Meanwhile, the analysis of Vernier/main scales on all 4 sides shows a misalignment of ±0.5 μm (Fig. 7C). For moiré-fringe analysis, on each side, the results of inner and outer areas are well matched (Fig. 7D) with the calculated misalignment from each region in Table 2. The misalignments in *x*, *y*, and rotation calculated from both areas are shown in Table 3. Based on the results from the outer area, the misalignments are 4.3 nm in *x*, −4.1 nm in *y*, and 71.5 μrad in rotation. The residual inaccuracy of the calculated results was attributed to sampling resolution and signal-to-noise ratio.

Table 2. Experimentally determined mismatch in each region using moiré-fringe analysis

	Inner area (M_{mi} = 31.3)		Outer area (M_{mo} = 62.5)	
Region	Δ_i (μm)	δ_i (nm)	Δ_o (μm)	δ_o (nm)
Top	−0.34	−2.6	−1.92	−7.4
Bottom	4.56	35.0	4.15	15.9
Left	−2.9	−22.7	7.44	28.6
Right	−1.42	−10.9	−9.55	−36.7

Gluing process

Before the fine alignment of *x*, *y*, and rotation, a UV light adhesive (Norland Products, NOA63) was injected into the left and right gaps between the 2 chips by using a syringe with a 30-gauge needle. After the completion of the alignment procedure, 365-nm UV light illuminated the chips for 10 min to cure the adhesive. Changes in *x*, *y*, and rotation were monitored and compensated for during the gluing process. After the 2 chips were glued, the assembly was lifted and detached from the bottom chip holder.

Discussion

We have developed the DIANA system that enables stacking 2 x-ray FZP chips with nanometer-level accuracy in a noncontact manner. The meticulous pattern design combined with coherent and incoherent illumination leverages the characteristics of the x-ray FZP chips, allowing the integration of laser interferometry, geometric image alignment, and moiré-fringe metrology for accurate control of the positions of both chips in 5 degrees of freedom. This system has demonstrated alignment accuracy of sub-30 nm in the *x* and *y* directions and 100 μrad in rotation.

Future work will be carried out in the aspects of system improvement and application exploration. In particular, we plan to continue developing the control software and integrate a robotic arm into the DIANA system to fully automate the alignment and gluing procedure. We will also explore the implementation of other light sources (e.g., a superluminescent diode) to control the movement in the *z* direction. These improvements will facilitate the ultimate objective of retrofitting the DIANA system into a nanofabrication facility with a stable mass production ability of high-diffraction-efficiency stacked FZPs. Toward this goal, we plan to use an x-ray microscope to examine the stacked FZPs. We will also test their efficiency compared with that of single FZPs using x-ray diffraction. In particular, an order-sorting aperture and a center stop aperture will be used to block x-rays of diffraction orders other than the first order. Efficiency will be calculated using the intensity of the first-order diffraction divided by the total intensity through the area of the FZP stack. From simulations [60], the stacking of two 750-nm-thick FZPs could enhance the diffraction efficiency from 14.1% to 30.1% at a photon energy of 8.39 keV. Thus, experimentally, the goal of x-ray inspection is to observe an increase in diffraction efficiency from the practical diffraction efficiency (i.e., 5%

Table 3. Calculated misalignments of *x*, *y*, and rotation

		Misalignment		
Approach		*x* (nm)	*y* (nm)	Rotation (μrad)
Vernier/main scales		[−500, 500]	[−500, 500]	[−1,250, 1,250]
Moiré fringes	Inner area	16.2	−16.8	−29.3
	Outer area	4.3	−4.1	−71.5

to 10%) of a single FZP. Moreover, we will explore the possibility of stacking 2 stacked FZP pairs to further improve the diffraction efficiency at higher photon-energy levels. As a generic all-optical nanoalignment platform, DIANA can be readily applied to other applications, including the stacking of double-sided FZPs to further enhance the aspect ratio, the generation of a multi-level FZP via alignment of multiple binary FZPs with different feature sizes, and the construction of an optical diffractive neural network by accurately assembling diffractive optical elements.

Acknowledgments

Funding: This work was supported in part by the Natural Sciences and Engineering Research Council of Canada (grant numbers: RGPIN-2024-05551 and ALLRP 585228-23), Mitacs Accelerate (grant number: IT36040), Canada Research Chairs Program (grant number: CRC-2022-00119), and Fonds de recherche du Québec–Nature et technologies (grant number: 203345 - Centre d'optique, photonique et lasers).
Author contributions: S.W. built the system, developed system automation and image processing algorithms, performed the experiments, and analyzed the data. C.J. contributed to the early-stage development and experiments. R.P. and M.A. fabricated x-ray FZPs with alignment markers and analyzed the data. J.L., R.P., and M.A. initiated the project. J.L. conceived the concept, contributed to system design, and supervised the project. All authors wrote and revised the paper.
Competing interests: The authors disclose the patent application U.S. Provisional 63/605,290.

Data Availability

All data are available from the corresponding author upon reasonable request.

Supplementary Materials

Notes S1 and S2
Figs. S1 and S2

References

1. Anderson EH, Olynick DL, Harteneck B, Veklerov E, Denbeaux G, Chao W, Lucero A, Johnson L, Attwood D. Nanofabrication and diffractive optics for high-resolution x-ray applications. *J Vac Sci Technol B*. 2000;18(6):2970–2975.
2. Wu S-R, Hwu Y, Margaritondo G. Hard-X-ray zone plates: Recent progress. *Materials*. 2012;5(10):1752–1773.
3. Snigirev A, Kohn V, Snigireva I, Lengeler B. A compound refractive lens for focusing high-energy X-rays. *Nature*. 1996;384:49–51.
4. Seiboth F, Schropp A, Scholz M, Wittwer F, Rödel C, Wünsche M, Ullsperger T, Nolte S, Rahomäki J, Parfeniukas K, et al. Perfect X-ray focusing via fitting corrective glasses to aberrated optics. *Nat Commun*. 2017;8:Article 14623.
5. Koch RJ, Jozwiak C, Bostwick A, Stripe B, Cordier M, Hussain Z, Yun W, Rotenberg E. Nano focusing of soft X-rays by a new capillary mirror optic. *Synchrotron Radiat News*. 2018;31(4):50–52.
6. Kumakhov MA. Capillary optics and their use in x-ray analysis. *X-Ray Spectrom*. 2000;29(5):343–348.
7. Hudec R. Kirkpatrick-Baez x-ray optics: A review. In: Hudec R, Pina L, editors. *EUV and X-ray optics: Synergy between laboratory and space II*. Bellingham (WA): SPIE; 2011. p. 62–75.
8. Mimura H, Handa S, Kimura T, Yumoto H, Yamakawa D, Yokoyama H, Matsuyama S, Inagaki K, Yamamura K, Sano Y, et al. Breaking the 10 nm barrier in hard-X-ray focusing. *Nat Phys*. 2010;6:122–125.
9. Conley R, Bouet N, Chu YS, Huang X, Kang HC, Macrander AT, Maser J, Nazaretski E, Stephenson GB, Yan H. Multilayer Laue lens: A brief history and current status. *Synchrotron Radiat News*. 2016;29(4):16–20.
10. Bajt S, Prasciolu M, Fleckenstein H, Domaracký M, Chapman HN, Morgan AJ, Yefanov O, Messerschmidt M, Du Y, Murray KT, et al. X-ray focusing with efficient high-NA multilayer Laue lenses. *Light Sci Appl*. 2018;7:Article 17162.
11. Lider V. Zone plates for X-ray focusing (review). *J Surf Investig*. 2017;11:1113–1127.
12. Ice GE, Budai JD, Pang JW. The race to x-ray microbeam and nanobeam science. *Science*. 2011;334(6060):1234–1239.
13. Lider VV. X-ray microscopy. *Physics-Uspekhi*. 2017;60(2): 187–203.
14. Geilhufe J, Pfau B, Schneider M, Büttner F, Günther CM, Werner S, Schaffert S, Guehrs E, Frömmel S, Kläui M, et al. Monolithic focused reference beam X-ray holography. *Nat Commun*. 2014;5:Article 3008.
15. Pascarelli S, Mathon O, Munoz M, Mairs T, Susini J. Energy-dispersive absorption spectroscopy for hard-X-ray micro-XAS applications. *J Synchrotron Radiat*. 2006;13(Pt 5):351–358.
16. Solak HH. Nanolithography with coherent extreme ultraviolet light. *J Phys D*. 2006;39:Article R171.
17. Zhang H, Liu H, Xu W, Lu Z. Large aperture diffractive optical telescope: A review. *Opt Laser Technol*. 2020;130:Article 106356.
18. Gleber S-C, Wojcik M, Liu J, Roehrig C, Cummings M, Vila-Comamala J, Li K, Lai B, Shu D, Vogt S. Fresnel zone plate stacking in the intermediate field for high efficiency focusing in the hard X-ray regime. *Opt Express*. 2014;22(23): 28142–28153.
19. Hémonnot CY, Köster S. Imaging of biological materials and cells by X-ray scattering and diffraction. *ACS Nano*. 2017;11(9):8542–8559.
20. Tamura S, Yasumoto M, Kamijo N, Suzuki Y, Awaji M, Takeuchi A, Uesugi K, Terada Y, Takano H. New approaches to fabrication of multilayer Fresnel zone plate for high-energy synchrotron radiation X-rays. *Vacuum*. 2006;80(7):823–827.
21. Chen Y. Nanofabrication by electron beam lithography and its applications: A review. *Microelectron Eng*. 2015;135:57–72.
22. Nöhammer B, Hoszowska J, Herzig H-P, David C. Zoneplates for hard X-rays with ultra-high diffraction efficiencies. *J Phys IV France*. 2003;104:193–196.
23. Sanli UT, Jiao C, Baluktsian M, Grévent C, Hahn K, Wang Y, Srot V, Richter G, Bykova I, Weigand M, et al. 3D nanofabrication of high-resolution multilayer Fresnel zone plates. *Adv Sci*. 2018;5(9):Article 1800346.
24. Keskinbora K, Robisch AL, Mayer M, Sanli UT, Grévent C, Wolter C, Weigand M, Szeghalmi A, Knez M, Salditt T, et al. Multilayer Fresnel zone plates for high energy radiation resolve 21 nm features at 1.2 keV. *Opt Express*. 2014;22(15):18440–18453.
25. Je JH, Jung J. Method for manufacturing X-ray/γ-ray focusing optical system using atomic layer deposition. 2024; US11919264B2.
26. Kamijo N, Suzuki Y, Takano H, Tamura S, Yasumoto M, Takeuchi A, Awaji M. Microbeam of 100 keV x ray with

a sputtered-sliced Fresnel zone plate. *Rev Sci Instrum*. 2003;74(12):5101–5104.
27. Sanli UT, Keskinbora K, Grévent C, Schütz G. Overview of the multilayer-Fresnel zone plate and the kinoform lens development at MPI for intelligent systems. In: Hudec R, Pina L, editors. *EUV and X-ray optics: Synergy between laboratory and space IV*. Bellingham (WA): SPIE; 2015. p. 248–256.
28. Mayer M, Keskinbora K, Grévent C, Szeghalmi A, Knez M, Weigand M, Snigirev A, Snigireva I, Schütz G. Efficient focusing of 8 keV X-rays with multilayer Fresnel zone plates fabricated by atomic layer deposition and focused ion beam milling. *J Synchrotron Radiat*. 2013;20 (Pt 3):433–440.
29. Mohacsi I, Vartiainen I, Rösner B, Guizar-Sicairos M, Guzenko VA, McNulty I, Winarski R, Holt MV, David C. Interlaced zone plate optics for hard X-ray imaging in the 10 nm range. *Sci Rep*. 2017;7:Article 43624.
30. Chang C, Sakdinawat A. Ultra-high aspect ratio high-resolution nanofabrication for hard X-ray diffractive optics. *Nat Commun*. 2014;5:Article 4243.
31. Maser J, Lai B, Yun W, Shastri SD, Cai Z, Rodrigues W, Xu S, Trackhtenberg E. Near-field stacking of zone plates in the x-ray range. In: Mancini SC, editor. *Design and microfabrication of novel X-ray optics*. Bellingham (WA): SPIE; 2002. p. 74–81.
32. Aristov V, Isoyan A, Kohn V, Kuyumchyan A, Shulakov E, Snigirev A, Snigireva I. Study of optical properties of x-ray system based on two zone plates. *Nucl Instrum Methods Phys Res A*. 2007;575(1–2):238–241.
33. Werner S, Rehbein S, Guttmann P, Heim S, Schneider G. Towards high diffraction efficiency zone plates for X-ray microscopy. *Microelectron Eng*. 2010;87(5–8):1557–1560.
34. Werner S, Rehbein S, Guttmann P, Schneider G. Three-dimensional structured on-chip stacked zone plates for nanoscale X-ray imaging with high efficiency. *Nano Res*. 2014;7:528–535.
35. Mohacsi I, Vartiainen I, Guizar-Sicairos M, Karvinen P, Guzenko VA, Müller E, Färm E, Ritala M, Kewish CM, Somogyi A, et al. High resolution double-sided diffractive optics for hard X-ray microscopy. *Opt Express*. 2015;23(2): 776–786.
36. Yurgens V, Koch F, Scheel M, Weitkamp T, David C. Measurement and compensation of misalignment in double-sided hard X-ray Fresnel zone plates. *J Synchrotron Radiat*. 2020;27(Pt 3):583–589.
37. Shastri S, Maser J, Lai B, Tys J. Microfocusing of 50 keV undulator radiation with two stacked zone plates. *Opt Commun*. 2001;197(1–3):9–14.
38. Li K, Jacobsen C. More are better, but the details matter: Combinations of multiple Fresnel zone plates for improved resolution and efficiency in X-ray microscopy. *J Synchrotron Radiat*. 2018;25(Pt 4):1048–1059.
39. Feng Y, Feser M, Lyon A, Rishton S, Zeng X, Chen S, Sassolini S, Yun W. Nanofabrication of high aspect ratio 24nm x-ray zone plates for x-ray imaging applications. *J Vac Sci Technol B*. 2007;25(6):2004–2007.
40. Snigireva I, Snigirev A, Kohn V, Yunkin V, Grigoriev M, Kuznetsov S, Vaughan G, Michiel MD. Hard X-ray focusing by stacked Fresnel zone plates. In: Khounsary AM, Morawe C, Goto S, editors. *Advances in X-ray/EUV optics and components II*. Bellingham (WA): SPIE; 2007. p. 117–127.
41. Wojcik MJ, Gleber S-C, Shu D, Roehrig C, Lai B, Vine D, Vogt S. Stacking multiple zone plates for efficient hard x-ray focusing at the advanced photon source. In: Lai B, editor. *X-ray nanoimaging: Instruments and methods II*. Bellingham (WA): SPIE; 2015. p. 48–56.
42. Snigireva I, Snigirev A, Kohn V, Yunkin V, Grigoriev M, Kuznetsov S, Vaughan G, di Michiel M. Focusing high energy X-rays with stacked Fresnel zone plates. *Phys Status Solidi A*. 2007;204(8):2817–2823.
43. Creath K, Wyant J. Moiré and fringe projection techniques. In: Malacara D, editor. *Optical shop testing*. New York (NY): Wiley; 1992. Vol. 2. p. 653–685.
44. Liu M, Wang L, Yu G. Developing graphene-based Moiré heterostructures for twistronics. *Adv Sci*. 2022;9(1):Article 2103170.
45. Reid GT. Moiré fringes in metrology. *Opt Laser Eng*. 1984;5(2):63–93.
46. Jiang W, Wang H, Xie W, Qu Z. Lithography alignment techniques based on moiré fringe. *Photonics*. 2023;10(4):Article 351.
47. Coltharp C, Xiao J. Superresolution microscopy for microbiology. *Cell Microbiol*. 2012;14(12):1808–1818.
48. Wang C, Taniyama S, Wang Y-H, Suga T. High-precision alignment for low-temperature wafer bonding. *J Electrochem Soc*. 2009;156:Article H197.
49. Wang C, Suga T. Measurement of alignment accuracy for wafer bonding by moiré method. *Jpn J Appl Phys*. 2007;46: 1989–1993.
50. Ghazanfarian AA, Chen X, McCord MA, Fabian R, Pease W, Nguyen K, Levinson H. Exploiting structure of wafer distortion in global alignment. *J Vac Sci Technol B*. 1998;16:3642–3646.
51. Mühlberger M, Bergmair I, Schwinger W, Gmainer M, Schöftner R, Glinsner T, Hasenfuß C, Hingerl K, Vogler M, Schmidt H, et al. A Moiré method for high accuracy alignment in nanoimprint lithography. *Microelectron Eng*. 2007;84 (5–8):925–927.
52. Zhu J, Hu S, Yu J, Tang Y. Alignment method based on matched dual-grating moiré fringe for proximity lithography. *Opt Eng*. 2012;51(11):Article 113603.
53. Li N, Wu W, Chou SY. Sub-20-nm alignment in nanoimprint lithography using Moiré fringe. *Nano Lett*. 2006;6(11): 2626–2629.
54. Batzer A-K. Optical alignment method for stacking high resolution zone plates [thesis]. [Stockholm (Sweden)]: KTH Royal Institute of Technology; 2015.
55. Kwan A. Vernier scales and other early devices for precise measurement. *Am J Phys*. 2011;79(4):368–373.
56. Snigireva I, Snigirev A, Vaughan G, Michiel MD, Kohn V, Yunkin V, Grigoriev M. Stacked Fresnel zone plates for high energy x-rays. *AIP Conf Proc*. 2007;879(1):998–1001.
57. Zhu J, Hu S, Yu J, Zhou S, Tang Y, Zhong M, Zhao L, Chen M, Li L, He Y, et al. Four-quadrant gratings moiré fringe alignment measurement in proximity lithography. *Opt Express*. 2013;21(3):3463–3473.
58. Jiang C, Kilcullen P, Lai Y, Ozaki T, Liang J. High-speed dual-view band-limited illumination profilometry using temporally interlaced acquisition. *Photonics Res*. 2020;8(11):1808–1817.
59. Liang J, Kohn RN, Becker MF, Heinzen DJ. Homogeneous one-dimensional optical lattice generation using a digital micromirror device-based high-precision beam shaper. *J Micro Nanolithogr MEMS MOEMS*. 2012;11(2):Article 023002.
60. Applied Nanotools Inc. Zone plate calculator. Applied Nanotools Inc. 2024. [accessed 26 Jan 2025] https://www.appliednt.com/zpcalc/